4D Maximum *A Posteriori* Reconstruction in Dynamic SPECT Using a Compartmental Model-Based Prior

Dan J. Kadrmas and **Grant T. Gullberg**
Utah Center for Advanced Imaging Research, Department of Radiology, University of Utah, 729 Arapeen Dr., Salt Lake City, UT 84108-1218, kadrmas@ucair.med.utah.edu

Abstract

A 4D ordered-subsets maximum *a posteriori* (OSMAP) algorithm for dynamic SPECT is described which uses a temporal prior that constrains each voxel's behavior in time to conform to a compartmental model. No *a priori* limitations on kinetic parameters are applied; rather, the parameter estimates evolve as the algorithm iterates to a solution. The estimated parameters and time-activity curves are used within the reconstruction algorithm to model changes in the activity distribution as the camera rotates, avoiding artifacts due to data inconsistencies between projection views. This potentially allows for fewer, longer duration scans to be used and may have implications for noise reduction. The algorithm was evaluated qualitatively using dynamic ^{99m}Tc-teboroxime SPECT scans in two patients, and quantitatively using a series of simulated phantom experiments. The OSMAP algorithm resulted in images with better myocardial uniformity and definition, gave time-activity curves with reduced noise variations, and provided wash-in parameter estimates with better accuracy and lower statistical uncertainty than those obtained from conventional ordered-subsets expectation-maximization (OSEM) processing followed by compartmental modeling. The new algorithm effectively removed the bias in k_{21} estimates due to inconsistent projections for sampling schedules as slow as 60 sec. per timeframe, but no improvement in washout parameter estimates was observed in this work. The proposed dynamic OSMAP algorithm provides a flexible framework which may benefit a variety of dynamic tomographic imaging applications.

1. INTRODUCTION

Conventional imaging with single-photon emission computed tomography (SPECT) involves acquiring projection data of radiopharmaceutical distributions that are assumed to be fixed over the duration of the scan. Physiological processes are dynamically changing, however, and the kinetics of radiotracer uptake and redistribution can provide quantitative measures of physiological processes that furnish more information than is available from static imaging. Dynamic imaging with positron emission tomography (PET) is a well-established methodology (Huang and Phelps 1986). More recently, developments in SPECT imaging agents and camera hardware have sparked interest in performing dynamic imaging with that modality (Budinger *et al.* 1991, Nakajima *et al.* 1991, Chiao *et al.* 1994b, Smith and Gullberg 1994, Gullberg *et al.* 1998, Iida and Eberl 1998, Lau *et al.* 1998). Dynamic imaging with SPECT is more difficult than it is with PET for a variety of reasons. In particular, the use of rotating gamma cameras limits temporal sampling rates and leads to data inconsistencies between projection angles (Links *et al.* 1991, Smith and Gullberg 1994, Welch *et al.* 1995, Ross *et al.* 1997, Lau *et al.* 1998). Likewise, the relatively high levels of statistical noise greatly limit the confidence with which kinetic parameters can be estimated (Huesman and Mazoyer 1987, Kadrmas *et al.* 1999, Welch *et al.* 1995). The sampling and data inconsistency problems can be reduced by using fast serial acquisitions (down to 5s. per 360° scan with a 3-head camera), but this results in very large datasets, provides very low statistics for each timeframe, and precludes the use of contoured orbits. From a practical standpoint slow rotation protocols

are desirable, and they may be the only feasible option when multi-head cameras are not available. However, slow rotation protocols result in poor temporal sampling at the tomographic level and enhance the data inconsistency problem.

Recent efforts in dynamic SPECT research have sought to mitigate the problem of inconsistent projections while utilizing the faster temporal sampling that occurs at the level of individual projection views, as opposed to full tomographic scans. Many researchers have investigated bypassing the image reconstruction step and estimating kinetic parameters directly from projection data (Chiao *et al.* 1994a, Limber *et al.* 1994, Zeng *et al.* 1995, Matthews *et al.* 1997, Huesman *et al.* 1998, Meikle *et al.* 1998, Reutter *et al.* 1998, Bauschke *et al.* 1999, Sitek *et al.* 1999). Since the tomographic sampling must be decoded in these schemes, it may be more accurate to say that the reconstruction and parameter estimation steps have been combined instead of the reconstruction step bypassed. The work presented here falls along similar lines, though tomographic reconstruction remains an explicit feature of the proposed data processing scheme.

Kinetic parameter estimation from dynamic tomographic data is a problem especially receptive to maximum *a posteriori* (MAP) reconstruction methods—the nature of the problem presupposes *a priori* knowledge of the form of the solution, *i.e.* that the temporal behaviors of the reconstructed image voxels obey a compartmental model. We propose a MAP algorithm for reconstructing dynamic SPECT data that uses a temporal prior based upon a compartmental model for tracer kinetics. The algorithm is four-dimensional (3D spatial plus time) and reconstructs each timeframe of the serial acquisition simultaneously; a related 4D algorithm was previously proposed by Lalush and Tsui (1998) for the reconstruction of gated SPECT data. The temporal prior encourages the time behavior of image values to match a compartmental model. It also provides a means for modeling how the tracer distribution changes as the camera rotates during the acquisition, thereby addressing the inconsistent projection problem. The prior can be applied on a voxel-by-voxel or regional basis, and it introduces a degree of temporal smoothing on the time-activity curve (TAC) for each voxel, potentially reducing the effects of statistical noise. Calculation of the temporal prior term involves finding the best fit TAC for the compartmental model at each iteration. This results in kinetic parameter estimates that evolve as the algorithm iterates toward a solution, bearing many similarities with parametric reconstruction algorithms (Carson and Lange 1985, Meikle *et al.* 1998). The framework is also well-suited for accepting spatially regularizing priors, and such priors could readily be applied to either reconstructed voxel intensities or kinetic parameter estimates as desired.

In this paper we describe the 4D MAP reconstruction algorithm with compartmental-model based prior and model for the inconsistent projection phenomenon, and implement it using an ordered-subsets approach. Initial evaluation of the 4D OSMAP algorithm is then performed using two patient studies and a series of simulation experiments for dynamic cardiac SPECT imaging of Tc-99*m* teboroxime (Stewart *et al.* 1990, Bontemps *et al.* 1991, Nakajima *et al.* 1991, Leppo *et al.* 1991, Chua *et al.* 1993, Smith *et al.* 1996). Teboroxime is a neutral lipophilic compound with high myocardial extraction and rapid washout kinetics, making it well-suited for dynamic imaging. The wash-in rate parameter for teboroxime has been shown to correlate well with perfusion, and may potentially provide a quantitative measure of myocardial perfusion *in vivo* using dynamic SPECT imaging. Imaging of other tracers was not evaluated in this work. The bias and noise properties of the new algorithm for the teboroxime imaging application are studied and compared with the conventional dynamic image processing method.

2. ALGORITHM DESCRIPTION

Let $\hat{x}$ and $\tilde{p}$ be vectors representing the image voxels and projection measurements, respectively, including all timeframes of the dynamic acquisition. Baye's equation relates the *a posteriori* probability distribution $P(\hat{x}|\tilde{p})$ to the likelihood function $P(\tilde{p}|\hat{x})$:

$$P(\hat{x}|\tilde{p}) = P(\tilde{p}|\hat{x}) \bullet P(\hat{x}) \div P(\tilde{p}) ,\tag{1}$$

where $P(\hat{x})$ and $P(\tilde{p})$ are the *a priori* probability distributions of the images and projection measurements, respectively. Let T be the number of individual scans acquired in the dynamic sequence; *i.e.*, T is the number of timeframes. The vector $\hat{x}$ has NT elements, where N is the number of voxels in a single 3D image; likewise $\tilde{p}$ has MT elements, where M is the number of projection image pixels acquired per individual scan (equal to the number of bins × slices × angles). The measurements $\tilde{p}$ should be normalized to units of either activity or counts per second. In the following discussion, we index the images and measurements as follows: the ith element of $\hat{x}$ is related to spatial voxel j and timeframe n by $i = j + (n-1)N$; likewise, the mth element of $\tilde{p}$ is related to projection image pixel l and timeframe n by $m = l + (n-1)M$.

In the following subsections we discuss the prior, $P(\hat{x})$, which incorporates the compartmental-model, and then the likelihood function will be described with the added feature of modeling the dynamic changes in activity distribution in order to compensate for the inconsistent projection phenomenon. We use the conventions that a tilde (~) denotes measured values, a caret (ˆ) indicates a quantity that is–or will be–estimated from the measurements, and a bar (¯) signifies that the value results from a fit to the estimated data.

One key, and rather unique, property of the proposed algorithm is the notion of reconstructing images that represent *instantaneous* activity distributions in time. Generally, tomographic data are reconstructed to provide images that represent the average or integral activity distribution over the time during which the scan was acquired. When using a 4D reconstruction algorithm that uses continuous analytical models for each voxel's temporal behavior, it is possible to reconstruct "instantaneous" estimates of the activity distribution at given points along the modeled time-activity curves. However, though the reconstructed images represent the activity distribution at given instants in time, the highest temporal frequency that can be reconstructed by the algorithm is limited by the temporal sampling rate of the measurements. In our case, this rate is given by the acquisition time of individual projection angles. This frequency is generally much higher than what is needed to accurately represent the time-activity curves of most tracers, but utilization of higher sampling rates is helpful in compensating for the inconsistent projection phenomenon. We have chosen to reconstruct one timeframe for each full tomographic acquisition, though the proposed algorithm has considerable flexibility for reconstructing additional timepoints as well. In order to minimize the temporal distance from the reconstructed timepoint to the time that each projection view was acquired, images in this work were reconstructed at the times corresponding to the midpoint of each individual scan. The reasons for reconstructing instantaneous activity estimates are somewhat subtle but will become evident with further examination of the algorithm and its implementation.

2.1. Compartmental-Model Based Prior

The foundation of the proposed 4D MAP algorithm is the compartmental-model based temporal prior. We describe the prior as applied on a voxel-by-voxel basis; the framework can easily be extended for priors defined for groups of voxels, or to eliminate the prior for some voxels. A time-activity curve vector can be described for each spatial voxel j at each iteration by collecting the reconstructed activity estimates of the voxel over time:

$$\widehat{TAC}(j) = \left\{ \widehat{x}_j, \widehat{x}_{j+N}, \ldots, \widehat{x}_{j+(T-1)N} \right\}.$$

(2)

Each $\widehat{TAC}(j)$ also includes the boundary condition that everything is zero prior to injection of the radiotracer. The temporal prior is chosen so that the most probable $\widehat{TAC}(j)$ is the one that best fits the compartmental model given the current image estimate. This is implemented by first fitting $\widehat{TAC}(j)$ to the compartmental model to obtain a set of parameters $\{k\rightarrow\}_j$ and a fitted curve $\overline{TAC}(j)$. The current implementation assumes that the input function is known *a priori, e.g.* from vascular sampling, by estimating it from projections (Sitek *et al.* 1999), or by other methods (DiBella *et al.* 1999). A potential function is then assigned for each space-time voxel i (spatial voxel j, timeframe n) such that the most probable value ($\bar{\mu}_i$) is given by the value of the fitted curve for that spatial voxel, $\overline{TAC}(j)$ at timepoint n. The choices for potential functions are numerous (Lange 1990), and we have heuristically chosen a Gaussian function:

$$P(\widehat{x}) = \prod_{i=1}^{NT} \frac{1}{\sqrt{2\pi}\sigma_i} e^{\frac{-(\widehat{x}_i - \bar{\mu}_i)^2}{2\sigma_i^2}},$$

(3)

where σ_i is the standard deviation of the distribution. Details on the selection of σ_i are given below. Note that $\bar{\mu}_i$ depends on the current image estimate, hence the prior probability distribution changes with iteration. The temporal prior encourages each $\widehat{TAC}(j)$ to match the compartmental model, but it does *not* assign *a priori* limitations on the rate parameters of the model. Thus the rate parameters evolve as the algorithm iterates toward a solution.

It is important to note that, unlike most previous applications of MAP reconstruction to emission computed tomography, the temporal prior of our 4D MAP algorithm encompasses long range features of the image (in time) and is not limited to local features only. This is significantly different than spatial smoothing priors that operate on 'cliques' of neighboring voxels. *A priori* knowledge of the temporal behavior of image values for all times, *e.g.* the expectation that they obey a compartmental model, makes such application of long range priors practicable. On a similar note, the temporal prior has an advantage over spatial smoothing priors in one respect. One of the difficulties of applying a spatial smoothing prior is the need to determine which voxels come from regions of nearly uniform intensity, and which voxels are separated by an 'edge' and should have greatly different values. The temporal prior has no such limitation since the *a priori* knowledge extends through all time, and therefore it is known that all timepoints on the time-activity curve are related.

2.2. Selection of Prior Weighting Parameters

As written in (3) above, σ_i must be specified for each timeframe and each voxel, and it is these parameters that determine the "weight" of the prior. We identify two components of these weighting parameters: $\sigma_i = \gamma\sigma_i'$, where σ_i' represents the relative uncertainty for each timepoint in $\widehat{TAC}(j)$, and γ is the overall weight of the prior. The inclusion of the relative uncertainties is useful because each TAC encompasses a wide range of values, the statistical uncertainty for each datum is related to the number of detected events arising from the voxel, and therefore it is related to the voxel intensity. Furthermore, nonlinear fitting to the compartmental-model—performed either within the OSMAP algorithm or as a post-processing step for conventional OSEM reconstruction—requires that the relative uncertainties for each datum be estimated. The selection of σ_i' is somewhat arbitrary, but it is also unlikely to have a dramatic effect upon the results. Ideally, σ_i' would be set equal to the statistical uncertainty of space-time voxel i for the current iteration and image estimate; however, this uncertainty is not known. We have set

each σ_i' equal to the square-root of TÂC(j) plus the mean value of TÂC(j) over all time points. The square-root term is based upon the assumption that the statistical uncertainty of each voxel is proportional to its intensity (Barrett *et al.* 1994; Wilson *et al.* 1994), and second term helps ensure that noisy voxels with low values do not receive disproportionately high weights.

The prior weighting factor, γ, must be selected for each imaging situation, and its optimal value may depend upon the count level, acquisition protocol, compartmental model, and other factors. The lack of optimal selection criteria for γ is currently a shortcoming of the dynamic MAP algorithm, and indeed most other MAP approaches. For the evaluations presented later in this paper, we varied γ for each reconstruction over a broad range and analyzed the dependencies of the resultant image quality upon γ. This is further described in the methods section. Further work should be performed in order to evaluate the optimal value of γ for each imaging situation.

2.3. Formulation of the Likelihood Function: Modeling Inconsistent Projections

The likelihood function, $P(\tilde{p}|\hat{x})$, relates the probability of obtaining the measurement $\tilde{p}$ given the image estimate, $\hat{x}$. In our case the activity distribution is known to be dynamically changing in time, hence the measurements for different timeframes, and indeed at different angles of the same timeframe, arise from different activity distributions. Furthermore, given *a priori* knowledge that each voxel's temporal behavior conforms to a compartmental model, it is possible to predict the activity distribution for each moment in time at which a projection angle was measured. Therefore a 4D dynamic model of the image can be used to calculate the likelihood function more accurately than in the more common case which assumes the activity distribution is static.

Recall that the number of photons acquired in a particular projection bin, $\tilde{p}_m$, is a random variable governed by Poisson statistics. The likelihood function can be written:

$$P(\tilde{p}|\hat{x})=\prod_{m=1}^{MT}e^{-\widehat{\tilde{p}}_m}\frac{\widehat{\tilde{p}}_m{}^{\tilde{p}_m}}{\tilde{p}_m!},$$

(4)

where $\tilde{p}_m$ is the mean of the Poisson distribution governing measurement in bin m given that the image is $\hat{x}$. In order to model changes in tracer activity as the camera rotates, $\tilde{p}_m$ is calculated using a time-dependent correction term, $\Delta\bar{x}_{i,m}$, which is calculated for each space-time voxel i and projection-time measurement m. Consider that the reconstructed image for timeframe n represents the instantaneous activity distribution at time t_n, but the projection measurements were acquired over some finite time interval around t_n. Let t_m' be the time at which projection measurement m was acquired (recall index m refers to projection pixel l of timeframe n). For shorter scan durations, the projection angle which measured pixel m may be treated as an instantaneous sample at time t_m'; however, for longer scans, the projection view may need to be treated as an integral over an interval in time, and an adjustment should be made accordingly. If $\mathbf{A}(t;\{k\!\rightarrow\}_j,\beta(t))$ is the solution to the compartmental modeling equation at time t for spatial voxel j, where $\{k\!\rightarrow\}_j$ are the fitted rate parameters for TÂC(j) and $\beta(t)$ is the blood input function, then the time-dependent correction term can be calculated as:

$$\Delta\bar{x}_{i,m}=\mathbf{A}\left(t\prime_m;\left\{\overrightarrow{k}\right\}_j,\beta(t)\right)-\mathbf{A}\left(t_n;\left\{\overrightarrow{k}\right\}_j,\beta(t)\right).$$

(5)

This quantity can then be added to the voxel for time t_n in order to predict what the activity in the voxel is at the time of measurement, t_m'.

Using the model for time-varying activity, the quantity $\hat{p}_m$ in the likelihood function is written:

$$\widehat{p}_m = \sum_{i=1}^{NT} F_{mi}(\widehat{x_i} + \Delta\overline{x}_{i,m}),$$

(6)

where F is the projection operator. Here F describes all source-to-measurement interactions and can be considered to be the imaging system transfer matrix. Each element F_{mi} is the probability that a photon emitted at source voxel location i would be detected in measurement bin m. Ideally, F should model for all aspects of the imaging system, including the depth-dependent detector response function, non-uniform attenuation, and scatter.

2.4. Expectation-Maximization Algorithm

Derivation of the expectation-maximization (EM) algorithm that maximizes eq. 1 requires two steps: formulation of the expectation of the natural logarithm of eq. 1 (using the complete-data likelihood function), and maximization of this expectation with respect to $\hat{x}$. The steps of this derivation are similar to those appearing in (Levitan and Herman 1987), and for the sake of brevity we present only the result of each major step here. We first introduce the complete data, $\tilde{z}_{i,m}$, which is the (unobservable) number of photons emitted from voxel i and detected in projection bin m. Instead of maximizing the conditional expectation of the incomplete data posterior probability function $P(\hat{x}|\tilde{p})$ directly, the MAP-EM algorithm maximizes the conditional expectation of the log of the complete data posterior probability function, $P(\hat{x}|\tilde{z})$. Hence, we need to write the complete data likelihood function, $P(\tilde{z}|\hat{x})$:

$$P(\tilde{z}|\widehat{x}) = \prod_{i=1}^{NT}\prod_{m=1}^{MT} e^{-F_{mi}(x_i\Delta\overline{x}_{i,m})} \frac{[F_{mi}(\widehat{x_i}+\Delta\overline{x}_{i,m})]^{\tilde{z}_{i,m}}}{\tilde{z}_{i,m}!}$$

(7)

Combining equation 3 and equation 7 according to Baye's relationship, the complete-data posterior probability function with the inconsistent projection model can be written as:

$$P(x|\tilde{z}) \prod_{i=1}^{NT}\prod_{m=1}^{MT} e^{-F_{mi}(\widehat{x_i}+\Delta\overline{x}_{i,m})} \frac{[F_{mi}(\widehat{x_i}+\Delta\overline{x}_{i,m})]^{\tilde{z}_{i,m}}}{\tilde{z}_{i,m}!} \bullet \prod_{i=1}^{NT} \frac{1}{\sqrt{2\pi}\sigma_i} e^{-\frac{(\widehat{x_i}-\overline{\mu}_i)^2}{2\sigma_i^2}} \div P(\tilde{z}).$$

(8)

The natural logarithm of eq. 8 is:

$$\ln[P(\widehat{x}|\tilde{z})] = \sum_{i=1}^{NT}\sum_{m=1}^{MT} \{\tilde{z}_{i,m}\ln[F_{mi}(\widehat{x_i}+\Delta\overline{x}_{i,m})] - F_{mi}(\widehat{x_i}+\Delta\overline{x}_{i,m}) - \ln(\tilde{z}_{i,m}!)\}$$
$$+ \sum_{i=1}^{NT}\left[\ln\left(\frac{1}{\sqrt{2\pi}\sigma_i}\right) - \frac{(\widehat{x_i}-\overline{\mu}_i)^2}{2\sigma_i^2}\right] - \ln[P(\tilde{z})]$$

(9)

The E-step involves taking the conditional expectation with respect to $\tilde{p}$ and the current image estimate, $\hat{x}^{old}$:

$$E_{\tilde{z}}\left[\ln P\left(\widetilde{x}|\tilde{z}\right)|\tilde{p},\widehat{x}^{\text{old}}\right] = \sum_{i=1}^{NT}\sum_{m=1}^{MT}\left\{N_{mi}\ln\left[F_{mi}\left(\widehat{x}_i+\Delta\overline{x}_{i,m}\right)\right] - F_{mi}\left(\widehat{x}_i+\Delta\overline{x}_{i,m}\right) - E_{\tilde{z}}\left[\ln\left(\tilde{z}_{i,m}!\right)|\tilde{p},\widehat{x}^{\text{old}}\right]\right\}$$
$$+\sum_{i=1}^{NT}\left[\ln\left(\frac{1}{\sqrt{2\pi}\sigma_i}\right) - \frac{\left(\widehat{x}_i-\overline{\mu}_i\right)^2}{2\sigma_i^2}\right] - E_{\tilde{z}}\left[\ln P\left(\tilde{z}\right)|\tilde{p},\widehat{x}^{\text{old}}\right],$$

(10)

where,

$$N_{mi} \equiv E_{\tilde{z}}\left[\tilde{z}_{i,m}|\tilde{p},\widehat{x}^{\text{old}}\right] = F_{mi}\left(\widehat{x}_i^{\text{old}}+\Delta\overline{x}_{i,m}^{\text{old}}\right)\frac{\tilde{p}_m}{\sum_{k=1}^{NT}F_{mk}\left(\widehat{x}_k^{\text{old}}+\Delta\overline{x}_{k,m}^{\text{old}}\right)}.$$

(10.1)

Here, N_{mi} is the conditional expectation of the complete data $\hat{z}_{i,m}$ given that the measurement $\tilde{p}$ has been made and that the image is $\widehat{x}^{\text{old}}$. The result (10.1) is obtained by recognizing that $\hat{z}_{i,m}$ is multinomially distributed given $\tilde{p}(\sum_{i=1}^{NT}\tilde{z}_{i,m}=\tilde{p}_m$, cells are i, number of trials is $\tilde{p}_m$, probability for each cell depends on F and $\widehat{x}^{\text{old}}$).

The M-step involves maximizing eq. (10) with respect to $\hat{x}$, which is accomplished by taking the partial derivative of eq. (10) with respect to $\hat{x}$ and setting the result equal to zero. This is done using the one-step late method of Green (Green 1990) to calculate the derivative, since elements of both the prior term ($\overline{\mu}_i$) and the model for inconsistent projections ($\Delta\overline{x}_{i,m}$) depend upon $\hat{x}$ in a complex manner. The final result is given by:

$$\widehat{x}_i^{\text{new}} = \frac{\overline{\mu}_i - \beta_i\sigma_i^2 + \left[\left(\overline{\mu}_i - \beta_i\sigma_i^2\right)^2 + 4\alpha_i\sigma_i^2\right]^{\frac{1}{2}}}{2},$$

(11)

where,

$$\alpha_i \equiv \widehat{x}_i^{\text{old}} \bullet \sum_{m=1}^{MT}F_{mi}\frac{\tilde{p}_m}{\sum_{k=1}^{NT}F_{mk}\left(\widehat{x}_k^{\text{old}}+\Delta\overline{x}_{i,m}^{\text{old}}\right)},$$

(11.1)

and

$$\beta_i \equiv \sum_{m=1}^{MT}F_{mi}.$$

(11.2)

One can verify that, when the weighting of the prior is set to zero ($\gamma, \sigma_i \to \infty$), the algorithm given in eq. 11 is equivalent to the maximum-likelihood expectation-maximization (MLEM) algorithm. Likewise, if the prior is given infinite weight ($\gamma, \sigma_i \to 0$), then eq. 11 converges in one step to the fitted TACs ($\hat{x}_i \to \overline{\mu}_i$). We make no attempt to prove convergence under other conditions, but empirical evidence from over 18 months use attest to satisfactory convergence in practice.

2.5. Ordered-Subsets Implementation

To speed the reconstruction, we have implemented the dynamic MAP-EM algorithm using an ordered-subsets (OS) approach (Hudson and Larkin 1994). The angles within each subset were equally spaced about the acquisition arc, and the subsets were ordered to maximize the angular distance between successive subsets. No effort was made to subset within timeframes in addition to within projection angles, though future optimizations of the algorithm should investigate this possibility. The following list summarizes the major steps of the OSMAP algorithm:

1. Form a 4D initial estimate image including all timeframes;

2. Extract TACs from the current image estimate for each region of the prior and f it to the compartmental-model;

3. Project the current image estimate to the current subset using the model for inconsistent projections based upon the compartmental-model fits obtained in step 2;

4. Compare the projected data to the measured data to get the errors;

5. Update the image estimate as in eq. (11); and

6. Repeat steps 2–5 until all subsets and iterations are traversed

3. EVALUATION METHODS

The new algorithm was used to process data from two patients which received dynamic cardiac SPECT scans with Tc-99m teboroxime. These data are presented as a reference point for practical implementation of the algorithm in a clinical setting, and provide a comparison between kinetic rate parameter estimates obtained using the new algorithm and more conventional processing with ordered-subsets expectation-maximization (OSEM) (Hudson and Larkin 1994). The bias and noise properties of the new algorithm were then quantitatively evaluated in detail using a series of simulated dynamic cardiac SPECT scans of Tc-99m-teboroxime. The simulation studies were also used to evaluate the effects of varying the prior weighting factor, γ, and to identify any gross differences in iterative convergence rate of OSMAP as compared to OSEM.

3.1. Patient Studies

Two patient with known coronary artery disease received dynamic cardiac SPECT scans on a three head IRIX gamma camera (Marconi Medical Systems) equipped with a Beacon™ transmission device and LEHR parallel-hole collimators. Two scans with Tc-99m teboroxime were acquired in each patient, one at rest and the other under pharmacologic stress. The teboroxime doses ranged from 629 to 1110 MBq (17 to 30 mCi) for these studies. The dynamic acquisition protocol consisted of acquiring 90 scans, each of 10 second duration, by rotating the 3-head camera successively clockwise and counter-clockwise through 120°. Each scan acquired 60 projection angles at 6° intervals using continuous gantry rotation. The scans were started 10–20 seconds prior to bolus injection of the radiotracer in order to ensure that the initial rise of activity was imaged. Transmission scans were acquired prior to each SPECT scan in order to obtain non-uniform attenuation maps so that attenuation compensation could be performed.

Imaging data was recorded onto 128 × 128 matrices using 0.467 cm pixels. The data were then reconstructed, first with 4 iterations of conventional OSEM, and then with 4 iterations of the OSMAP algorithm, both with 4 angles per subset. A prior weighting factor of $\gamma = 4.0$ was used for OSMAP; no specific optimization of this parameter was performed here, and the value chosen was based heuristically upon the results of the simulation studies described below. The effects of non-uniform attenuation and depth-dependent detector response were compensated

for by modeling them in both the projector and backprojector of the reconstruction algorithms (Tsui *et al.* 1998). The OSEM images were reoriented into short-axis slices, and then 8 symmetrical ROIs were drawn over the left ventricle (LV) wall on each of 7 adjacent pairs of short-axis slices for a total of 56 regions in all. No regions were drawn over the most basal or apical short axis slices. Each ROI was carefully drawn to include as much of the myocardium as possible while excluding background tissues; voxels which contained significant portions of myocardium and blood pool were generally included, as the blood pool effects are included within the compartmental model (f_v). The average ROI contained 26 voxels and contained a volume of 2.7cm^3. The blood input function was obtained by drawing a large (26.7cm^3) ROI on the LV blood pool. Time-activity curves were then calculated by applying the ROIs to each timeframe of the OSEM reconstructions, and the relative uncertainties for each data point were calculated in the same manner as described in the theory section for computing the OSMAP prior. The time-activity curves were fit to the two-compartment model shown in figure 1 using a modified Newton's method for function minimization in order to obtain wash-in and wash-out rate parameters for each region.

The OSMAP reconstructions were performed using the same ROIs as for the OSEM analysis, reoriented back to transaxial slices. Note that the OSMAP prior was only defined for voxels included in the LV ROIs, hence we expect the algorithm to impose regularization only in the vicinity of these ROIs and not across the entire image. The blood input function for the OSMAP reconstructions was also taken from the OSEM analysis. Since the OSMAP algorithm performs the compartmental-model fitting for each region internally at each iteration, the algorithm outputted reconstructed images and kinetic parameter estimates for each region directly.

3.2. Simulation Experiment

3.2.1. MCAT Phantom—The series of simulation experiments was performed using the mathematical cardiac torso (MCAT) phantom (Terry *et al.* 1990, Tsui *et al.* 1994). A static version of the phantom was first created, and time-activity curves were later assigned to each organ as described below to create a dynamic version of the phantom; this dynamic phantom is based on the static MCAT and should not be confused with other dynamic versions of the MCAT phantom such as the beating-heart phantom of Pretorius *et al.* (1997). The phantom had a 36×24 cm body contour with small breasts and was initially discretized onto a $256 \times 256 \times 128$ grid using cubic 0.178 cm voxels. The phantom was separated into five 'organs': blood, body, heart, liver and lungs; where 'blood' indicates the blood pools of the heart chambers, and 'body' includes the soft tissue background and all organs not otherwise specified. Sample images of the phantom organs and attenuation map for a transaxial slice through the middle of the heart are shown in figure 2.

3.2.2. Projection Data—Static projection data for each organ were calculated using a matrix-driven rotation-based projector that modeled the effects of non-uniform attenuation and depth-dependent collimator-detector response. The effects of scatter were not included in the simulation. The camera was modeled with a round-hole equivalent low-energy high resolution parallel hole collimator and had an intrinsic spatial resolution of 0.4 cm full-width at half maximum. A circular orbit was used with radius 19.0 cm to the front face of the collimator, and 120 projection angles were acquired at 3° intervals. The phantom images were first projected onto 256×128 projection matrices, and then collapsed to form 128×64 projection images with 0.356 cm pixels. This pixel size was used for all remaining image reconstruction and analysis.

3.2.3. Time-Activity Curves—Using the static versions of the MCAT phantom and simulated projection data, corresponding dynamic versions were created by weighting and summing the data for each organ according to simulated time-activity curves (TACs). Realistic

TACs were uniformly assigned to all voxels of each organ based upon dynamic teboroxime cardiac SPECT scans performed at our institution. The blood input function was modeled as the sum of three decaying exponentials preceded by a 10 second ramp function, mimicking a slow-bolus intravenous injection. The myocardium TAC was generated using the two compartment model shown in figure 1, where k_{21} and k_{12} are the wash-in and wash-out rate parameters, respectively, that describe exchange between the blood and extravascular tissue compartments (Smith 1994,Gullberg *et al.* 1998). The rate constants are functions of the permeability coefficient for flux out of and into the capillary (k_{ij}', unit of length/time), the volume per unit length of capillary (ϕ, unit of volume/length), and the volume of the exchanging compartment (V, unit of volume) as given by:

$$k_{ij} = \frac{k_{ij}' \cdot \phi}{V}.$$

(12)

The units of k_{21} and k_{12} are volume of exchanging blood in capillary per unit of time divided by the volume of the extravascular compartment (*i.e.*, ml/min/ml). Under this model, the activity concentration *A(t)* in the myocardium is related to the activity concentration in the blood, *B(t)*, and the kinetic parameters by:

$$A(t) = (1 - f_v)k_{21} \int_0^t e^{-k_{12}\tau} B(t - \tau)d\tau + f_v B(t),$$

(13)

where f_v is the vascular fraction in the myocardial region. Kinetic rate parameters of $k_{21} = 1.4$ ml/min/ml and $k_{12} = 0.5$ ml/min/ml were used for the simulations, and the vascular fraction within myocardial tissue was set to be 0.1. The simulated TACs for each organ of the dynamic phantom are plotted in figure 3.

3.2.4. Dynamic SPECT Acquisitions—The static projections for each organ were weighted by the corresponding TACs and summed one angle at a time in order to simulate serial SPECT acquisitions using a three head gamma camera. Four sets of acquisition protocols were simulated, ranging from fast rotation to slow rotation serial acquisitions: 60 scans @ 10 sec. each, 30 scans @ 20 sec. each, 20 scans @ 30 sec. each, and 10 scans @ 60 sec. each. Successive scans alternated between clockwise and counter-clockwise rotations of the gantry, which has some implications with respect to sampling but is required unless a camera with 'slip-ring' capability is available. Each individual scan had 120 projection angles evenly spaced over 360°. Note that the time at which each individual projection angle was acquired was calculated and used to determine the weighting factor for that view. This leads to inconsistent projection sets, as shown in figure 4, because the activity distribution changes as the camera rotates.

3.2.5. Statistics—Since each acquisition protocol used a total acquisition time of 10 minutes, the total count levels that would be acquired in practice for each protocol are nearly identical. The simulated noise-free projection sets were scaled to have approximately 800,000 total counts per typical cardiac slice over all time frames, and Poisson noise was simulated for each data set. The noisy data were then reconstructed and used to study the bias and noise properties of each data processing method as described below.

3.2.6. Reconstructions—The data for each acquisition protocol were reconstructed using three methods: (*i*) conventional OSEM reconstruction of each timeframe separately; (*ii*) 4D OSEM reconstruction using the model for inconsistent projections (identical to 4D OSMAP, but not using a Bayesian update); and (*iii*) 4D OSMAP reconstruction with both the inconsistent

projection model and Bayesian updates. Method (*ii*) provides a measure of the effectiveness of the inconsistent projection model separate from the Bayesian update scheme. Since the model requires knowledge of the predicted time-activity curves, the OSMAP reconstruction code was used; however, the "weight" of the prior was set to zero ($\gamma \to \infty$) so that OSEM updates were performed. For the OSMAP reconstructions, the prior was applied on a region-by-region basis as described in the next section so that each voxel in a given region shared the same prior. Both algorithms used 4 angles per subset, and model-based compensation for the effects of non-uniform attenuation and depth-dependent detector response was performed.

The OSMAP and OSEM algorithms may have different rates of iterative convergence, and it is important to account for this when comparatively evaluating the algorithms. We used the following stopping criterion: for each case studied, the number of iterations was chosen to maximize the accuracy-to-noise ratio (ANR) for k_{21} (see next section on data analysis) with the constraint that at least 3 iterations were performed in order to ensure suitable resolution recovery. For OSEM, the ANR for k_{21} was maximized using between 3 and 5 iterations for the different acquisition protocols studied. However, for OSMAP more iterations were required to maximize the ANR, and this number varied dependent upon the acquisition protocol used: 10 iterations for the 60×10 sec. protocol; 9 iterations for the 30×20 sec. protocol; 7 iterations for the 20×30 sec. protocol; and 3 iterations for the 60×10 sec. protocol.

The OSMAP reconstructions were repeated using numerous choices of the prior weighting factor, γ, ranging from 0.001 to 100. The results showed that the performance of the OSMAP algorithm was fairly insensitive to the choice of γ, and no significant changes in performance were observed for choices of γ on or about the same order of magnitude as its optimal value. Larger values of γ gave performance closer to OSEM, and smaller values of γ tended to slow iterative convergence so that more iterations were required. Based on this non-intensive search, we found the following values provided high (but not necessarily maximal) accuracy-to-noise ratios (as described in the next section): $\gamma = 0.1$ for the 60×10 sec. protocol; $\gamma = 0.7$ for the 30×20 sec. protocol; $\gamma = 0.75$ for the 20×30 sec. protocol; and $\gamma = 100$ for the 10×60 sec. protocol. Note that the value of γ for the slowest acquisition protocol was much higher than for the faster protocols. A value of $\gamma = 100$ gave slightly better results than $\gamma = 10$, but using values of $\gamma < 5$ led to greater levels of bias. We postulate that, due to the low number of timeframes for this slowest acquisition protocol, heavy weighting of the prior (*i.e.* $\gamma < 5$) slowed iterative convergence to the point that excessive bias remained in the images.

3.2.7. Data Analysis—Eight regions-of-interest (ROIs) were placed on each of 12 short-axis slices of the LV, for a total of 96 regions in all. Each region was drawn to encompass as much of the myocardial tissue as possible while excluding background tissues outside of the LV, though voxels containing part myocardium and part LV blood pool tended to be included in the ROIs. The mean ROIs size was 32.5 ± 14.6 voxels (1.47 ± 0.66 cm^3). Time-activity curves was calculated for each region by computing the mean voxel value in the ROI over all timeframes, and the resulting TACs were fit to the two compartment model to obtain estimates of k_{21}, k_{12}, and f_v. This fitting procedure is done automatically during reconstruction by the OSMAP algorithm, and it was done after reconstruction for the OSEM cases. No post-reconstruction smoothing filter was applied before calculating the kinetic rate parameters.

The mean and standard deviation of each rate parameter over the 96 regions was calculated for each acquisition protocol for both OSEM and OSMAP. The mean values were used to estimate the bias in the rate parameter estimates, and the standard deviations over the 96 regions were treated as measures of the statistical noise. As a combined measure of bias and noise, the

accuracy-to-noise ratio, $\text{ANR} \equiv \dfrac{\text{true value } - |\text{error}|}{\text{true value } + \text{s.d.}}$, was also calculated for each case.

4. RESULTS

4.1. Patient Studies

Figure 5 shows example transaxial images for a single timeframe of one of the dynamic cardiac SPECT patient studies reconstructed using conventional OSEM (no model for inconsistent projections) and the proposed OSMAP algorithm. The high levels of noise in the images are due to the very short acquisition time for this timeframe, only 10 sec. The images of figure 5 show differences in uniformity and definition of the myocardium, where the prior was defined, but these effects are difficult to visualize given the very high levels of statistical noise present in the images. As a measure of myocardial uniformity, we calculated the standard deviation over the 56 ROIs drawn on the myocardial wall. For the timeframe shown in figure 5, the inter-region standard deviation was 0.12 and 0.07 for OSEM and OSMAP, respectively. The average inter-region standard deviation over all timeframes was 0.015 for OSEM and 0.011 for OSMAP. These results show that the dynamic OSMAP algorithm produced images with better myocardial uniformity than did OSEM, which is due to the regularizing effect of the OSMAP algorithm. Note that this regularization occurs only in the temporal direction, and that no spatial regularization due to either Bayesian reconstruction or linear filtering has been applied to these images. Also note that the OSEM and OSMAP images appear very similar in the regions away from the LV where no OSMAP prior was defined. Similar qualitative effects were seen on the images of other timeframes (not shown).

Sample time-activity curves for a single ROI and both data processing schemes are given in figure 6. The TAC for the OSMAP algorithm shows markedly reduced noise variations as compared to the OSEM TAC. Similar effects were seen for the TACs from other regions. These data suggest that the OSMAP algorithm has successfully imposed a temporal regularization upon the reconstructed images due to the compartmental-model based prior.

In order to provide an example of the differences in kinetic parameter estimates obtained by the two data processing methods, scatter plots of the rate parameter estimates and distribution volumes ($V_d = k_{21}/k_{12}$) for OSMAP versus OSEM are given in figure 7. The data indicate that there is a strong correlation in rate parameter estimates for a large subset of the data, but there are also a fair number of regions for which the OSMAP algorithm gave parameter estimates substantially different than the OSEM estimates. The distribution volume was more stable in this regard but displayed similar behavior. These differences are likely due to the OSMAP algorithm's compensation for inconsistent projections and temporal regularization; however, since no gold standard for flow values was available for the patient studies, it cannot be determined from these data which algorithm gave more accurate results. We have performed a series of simulation experiments in order to address this issue.

4.2. Simulation Experiments

Example reconstructed images for the simulation experiments are shown in figure 8. The relative differences in image quality for the OSMAP versus OSEM reconstructions were similar to, but more pronounced than, those presented earlier for the patient studies, and the temporal smoothing of the time-activity curves imposed by OSMAP was also similar for both the simulation and patient studies. Note that, for the simulation studies, the prior was also defined for a large ROI drawn over the LV blood pool. The compartmental modeling equations still hold for this ROI due to the inclusion of the vascular fraction f_v (= 1.0 in this case). The images of figure 8 also show improved uniformity in the blood pool, demonstrating the regularizing effect of the prior even in blood-only regions.

The series of simulated phantom experiments was performed in order to quantitatively evaluate the bias and noise properties of the new algorithm as compared to conventional processing

with OSEM followed by compartmental modeling. The compartmental-model fit failed to converge for one ROI of the fastest acquisition protocol, hence this data point was excluded from the analysis. The estimated wash-in and wash-out parameters for each acquisition protocol and reconstruction method are summarized in Table I, and the mean values of each are plotted in figure 9. Scatter plots of OSMAP versus OSEM parameter estimates for the 60 × 10 sec. protocol are also provided in figure 10. There is less variability in the scatter plots for the simulation experiments (figure 10) as compared to for the patient data (figure 7), largely because the simulation study had a higher count level than did the patient data. However, in both cases the scatter plots indicate that there was some degree of correlation between rate parameters estimated by OSMAP versus OSEM, but the linear correlation analysis indicated some substantial differences between the two algorithms.

In order to evaluate these differences, a detailed quantitative analysis of the data in Table I was performed. Here, it was assumed that the parameters estimated for each of the 96 LV regions were independent samples of the myocardium, which was uniform in truth. The error in the mean values provides a measure of the bias in the rate parameters for each case, and the standard deviation over the 96 regions was considered to represent variability due to statistical noise. The accuracy-to-noise ratio was also calculated to provide a combined measure of bias and noise. Finally, a t-test was performed in order to test the hypothesis that the rate parameter estimates accurately represented the true values, versus the alternative that the parameter estimates were biased away from the true values. The attained significance levels are listed for cases that had significant bias, and the remaining cases are labeled NS (not significant), indicating that these parameter estimates were not significantly different from the true values.

The results of the simulation experiments show some interesting trends, both with respect to the data processing scheme applied as well as the dynamic acquisition protocol employed. In most cases the bias in the k_{21} estimates was lower for OSMAP versus conventional OSEM, and likewise the bias in k_{21} was lower for the OSEM reconstructions that used the model for inconsistent projections than for conventional OSEM. The statistical hypothesis tests demonstrated that there was no significant bias in OSMAP k_{21} estimates, whereas k_{21} estimates from conventional OSEM were significantly biased in two of the four cases studied. The accuracy-to-noise ratio measures for k_{21} showed an improvement for OSMAP versus OSEM in 3 out of 4 cases. These results indicate that the OSMAP model for inconsistent projections has achieved a fair degree of compensation, leading to more accurate wash-in rate parameter estimates. This was especially true when Bayesian updates were applied, though a lesser degree of compensation was achieved by the OSEM method which included the model for inconsistent projections.

Considering statistical noise, the uncertainties in the k_{21} estimates shown in Table I were higher for OSMAP than for OSEM. *However*, recall that these data were based upon stopping the iterative algorithms at the iteration number which maximized the ANR. More iterations were required to maximize the ANR for OSMAP than for OSEM. Though it turns out that the OSMAP uncertainties were higher than those for OSEM when using this stopping criterion, the ANR values for OSMAP were still better in 3 out of 4 cases. The ANR figure of merit used here provides only an example of the relative importance of bias and noise; in many instances the high levels of statistical noise encountered in dynamic SPECT necessitate the use of processing methods which sacrifice some degree of accuracy in exchange for a reduction in noise. In such cases, a different iterative stopping criterion would arise, and the OSMAP algorithm may provide k_{21} estimates with considerably lower standard deviations. Consider the plot of k_{21} standard deviation versus iteration number shown in figure 11. The OSMAP algorithm resulted in wash-in parameter estimates with substantially lower standard deviations at all iterations as compared to OSEM. Also note that the OSMAP results were more stable with iteration, which lessens the importance of optimizing the exact number of iterations to

use. We attribute these effects to the temporal regularization imposed by the OSMAP prior. It is likely that further reductions in noise effects could be obtained by adding spatial regularization as well, such as forming cliques of neighboring regions with similar kinetic behaviors.

The OSMAP algorithm had a different effect upon wash-out parameter estimates, where OSMAP k_{12} estimates tended to have somewhat higher bias than the OSEM k_{12} estimates. The exception was for the slowest acquisition protocol, for which OSMAP gave the k_{12} estimate with lowest bias. Interestingly, this was also the only case in which the bias in the k_{12} estimate was not statistically significant. The reasons that OSMAP provided worse performance for wash-out parameter estimates are not well understood. We have focused our efforts upon obtaining improved wash-in estimates, because k_{21} has been shown to be a much better measure of myocardial perfusion than k_{12} for dynamic teboroxime imaging (Smith and Gullberg 1994, Smith *et al.* 1996). Further work is required in order to evaluate the dynamic OSMAP algorithm for tracers in which washout parameter estimates are of greater interest.

5. DICSUSSION AND CONCLUSIONS

The OSMAP algorithm proposed in this work was specifically designed to address two of the difficulties associated with dynamic SPECT imaging, namely the issue of high statistical noise and the problem of data inconsistencies caused by dynamic changes in tracer distribution that occur during rotational acquisition. The algorithm addresses these difficulties by utilizing the expectation that the temporal behaviors of the reconstructed image voxels obey a compartmental-model for tracer kinetics within a Bayesian reconstruction framework. Though application of the new algorithm in this paper was limited to dynamic cardiac SPECT imaging with teboroxime, the OSMAP algorithm is readily applicable to other dynamic SPECT and dynamic PET imaging applications, and it may potentially bring the benefits of reduced noise and improved temporal modeling to such applications. In its current state, the algorithm requires *a priori* knowledge of the blood input function, obtainable *e.g.* from vascular sampling, by estimating it from projections, or by other methods. Note, also, that the algorithm is also applicable to dynamic imaging applications which do not use compartmental-modeling, *e.g.* those that use spectral mixture models, in which case the need for a blood input function may be obviated.

The algorithm was evaluated qualitatively using dynamic Tc-99m teboroxime SPECT scans in two patients, and quantitatively using a series of simulated phantom experiments. Promising results were obtained for wash-in rate parameter estimates, but wash-out parameter estimates were not improved. The reasons that the new algorithm failed to improve wash-out estimates are not fully understood, but we emphasize that the goal of this work was to improve wash-in estimates for dynamic teboroxime imaging, which have been shown to provide good correlation with flow. We conclude that the proposed algorithm is able to achieve some degree of compensation for the inconsistent projection phenomenon, and that its temporal regularization can provide wash-in parameter estimates with higher accuracy-to-noise ratios than those obtained with conventional OSEM processing. We emphasize that no direct spatial regularization was applied in this work, though the OSMAP framework readily lends itself to adding spatial cliques or other spatially regularizing priors. Further improvements may be effected by adding such spatial regularizations, and also by optimizing the weight of the prior for different imaging situations.

The simulation experiments included an analysis of the effects of using different acquisition protocols for dynamic teboroxime SPECT. Recall that fast sampling protocols provide better temporal sampling but very high levels of noise in each timeframe, whereas slower sampling protocols suffer from data inconsistencies between individual projection angles. The results of

this work demonstrate that the OSMAP algorithm effectively removed the bias in k_{21} estimates by compensating for inconsistent projections, a result which held true for each of the sampling protocols studied. The data also suggest that the 30×20 sec. acquisition protocol gave the best k_{21} estimates in term of accuracy-to-noise ratio, but further work would be required to exhaustively optimize the acquisition protocol for dynamic teboroxime SPECT.

Acknowledgments

REFERENCES

Barrett HH, Wilson DW, Tsui BMW. Noise properties of the EM algorithm: I. theory. Phys. Med. Biol 1994;39:833–846. [PubMed: 15552088]

Bauschke HH, Noll D, Celler A, Borwein JM. An EM algorithm for dynamic SPECT. IEEE Trans. Med. Imag 1999;18:252–261.

Bontemps L, Geronicola-Trapali X, Sayegh Y, Delmas O, Itti R, Andre-Fouet X. Technetium-99m teboroxime scintigraphy: clinical experience in patients referred for myocardial perfusion evaluation. Eur. J. Nucl. Med 1991;18:732–739. [PubMed: 1936049]

Budinger TF, Araujo L, Ranger N, Coxson P, Klein G, Huesman R, Alavi A. Dynamic SPECT feasibility studies (abstract). J. Nucl. Med 1991;32:955P.

Carson RE, Lange K. The EM parametric image reconstruction algorithm. J Am Statist Assoc 1985;80:20–22.

Chiao P-C, Rogers WL, Clinthorne NH, Fessler JA, Hero AO. Model-based estimation for dynamic cardiac studies using ECT. IEEE Trans. Med. Imag 1994a;13:217–226.

Chiao PC, Ficaro EP, Dayanikli F, Rogers WL, Schwaiger M. Compartmental analysis of technetium-99m-teboroxime kinetics employing fast dynamic SPECT at rest and stress. J. Nucl. Med 1994b;35:1265–1273. [PubMed: 8046477]

Chua T, Kiat H, Germano G, Takemoto K, Fernandez G, Biasio Y, Friedman J, Berman D. Rapid back to back adenosine stress-rest technetium-99m teboroxime myocardial perfusion SPECT using a triple-detector camera. J. Nucl. Med 1993;34:1485–1493. [PubMed: 8355068]

DiBella EVR, Clackdoyle R, Gullberg GT. Blind estimation of compartmental model parameters. Phys. Med. Biol 1999;44:765–780. [PubMed: 10211809]

Green PJ. Bayesian reconstructions from emission tomography data using a modified EM algorithm. IEEE Trans. Med. Imag 1990;9:84–93.

Gullberg, GT.; Huesman, RH.; Ross, SG.; Di Bella, EVR.; Zeng, GL.; Reutter, BW.; Christian, PE.; Foresti, SA. Dynamic cardiac single photon emission computed tomography. In: Zaret, BL.; Beller, GA., editors. Nuclear Cardiology: State of the Art and Future Directions. New York: Mosby-Year Book; 1998. p. 137-187.

Huang, SC.; Phelps, ME. Positron Emission Tomography and Autoradiography. Principles and Applications for the Brain and Heart. New York: Raven Press; 1986. Principles of tracer kinetic modeling in positron emission tomography and autoradiography.

Hudson HM, Larkin RS. Accelerated image reconstruction using ordered subsets of projection data. IEEE Trans. Med 1994;13:601–609.

Huesman RH, Mazoyer BM. Kinetic data analysis with a noisy input function. Phys. Med. Biol 1987;32:1569–1579. [PubMed: 3501592]

Huesman RH, Reutter BW, Zeng GL, Gullberg GT. Kinetic parameter estimation from SPECT cone-beam projection measurements. Phys. Med. Biol 1998;43:973–982. [PubMed: 9572520]

Iida H, Eberl S. Quantitative assessment of regional myocardial blood flow with thallium-201 and SPECT. J. Nucl. Cardiol 1998;5:313–331. [PubMed: 9669586]

Kadrmas DJ, DiBella EVR, Huesman RH, Gullberg GT. Analytical propagation of errors in dynamic SPECT: estimators, degrading factors, bias and noise. Phys. Med. Biol 1999;44:1997–2014. [PubMed: 10473210]

Lalush DS, Tsui BMW. Block-iterative techniques for fast 4D reconstruction using a priori motion models in gated cardiac SPECT. Phys. Med. Biol 1998;43:875–886. [PubMed: 9572511]

Lange K. Convergence of EM image reconstruction algorithms with Gibbs smoothing. IEEE Trans. Med. Imag 1990;9:439–446.

Lau C-H, Feng D, Hutton BF, Lun DP-K, Siu W-C. Dynamic imaging and tracer kinetic modeling for emission tomography using rotating detectors. IEEE Trans. Med. Imag 1998;17:986–994.

Leppo JA, DePuey EG, Johnson LL. A review of cardiac imaging with sestamibi and teboroxime. J. Nucl. Med 1991;32:2012–2022. [PubMed: 1833519]

Levitan E, Herman GT. A maximum *a posteriori* probability expectation maximization algorithm for image reconstruction in emission tomography. IEEE Trans. Med. Imag 1987;6:185–192.

Limber, MA.; Limber, MN.; Celler, A.; Barney, JS.; Borwein, JM. Direct reconstruction of functional parameters for dynamic SPECT. Proceedings of the 1994 IEEE Nuclear Science Symposium and Medical Imaging Conference; Norfolk, VA: IEEE Press; 1994. p. 1249-1256.

Links JM, Frank TL, Becker LC. Effect of differential tracer washout during SPECT acquisition. J. Nucl. Med 1991;32:2253–2257. [PubMed: 1824556]

Matthews J, Bailey D, Price P, Cunningham V. The direct calculation of parametric images from dynamic PET data using maximum-likelihood iterative reconstruction. Phys. Med. Biol 1997;42:1155–1173. [PubMed: 9194135]

Meikle SR, Matthew JC, Cunningham VJ, Bailey DL, Livieratos L, Jones T, Price P. Parametric image reconstruction using spectral analysis of PET projection data. Phys. Med. Biol 1998;43:651–666. [PubMed: 9533143]

Nakajima K, Taki J, Bunko H, Matsudaira M, Muramori A, Matsunari I, Hisada K, Ichihara T. Dynamic acquisition with a three-headed SPECT system: application to technetium 99m SQ30217 myocardial imaging. J. Nucl. Med 1991;32:1273–1277. [PubMed: 2045946]

Pretorius PH, Xia W, King MA, Tsui BMW, Pan TS, Villegas BJ. Evaluation of right and left ventricular volume and ejection fraction using a mathematical cardiac torso phantom for gated pool SPECT. J. Nucl. Med 1997;38:1528–1534. [PubMed: 9379187]

Reutter BW, Gullberg GT, Huesman RH. Kinetic parameter estimation from attenuated SPECT projection measurements. IEEE Trans. Nucl. Sci 1998;45:3007–3013.

Ross SG, Welch A, Gullberg GT, Huesman RH. An investigation into the effect of input function shape and image acquisition interval on estimates of washin for dynamic cardiac SPECT. Phys. Med. Biol 1997;42:2193–2213. [PubMed: 9394407]

Sitek, A.; Di Bella, EVR.; Gullberg, GT. Information Processing in Medical Imaging. Visegrad, Hungary: Springer-Verlag Berlin-Heidelberg; 1999. p. 436-441.(Ed. al., A. K. e.)

Smith, AM. Doctoral Dissertation. Salt Lake City, UT: Dept. of Bioengineering, University of Utah; 1994. Dynamic Cardiac SPECT Imaging.

Smith AM, Gullberg GT. Dynamic cardiac SPECT computer simulations for teboroxime kinetics. IEEE Trans. Nucl. Sci 1994;41:1626–1633.

Smith AM, Gullberg GT, Christian PE. Experimental verification of technetium-99m-labeled teboroxime kinetic parameters in the myocardium with dynamic single-photon emission computed tomography: reproducibility, correlation to flow, and susceptibility to extravascular contamination. J. Nucl. Cardiol 1996;3:130–142. [PubMed: 8799238]

Stewart RE, Schwaiger M, Hutchins GD, Chiao P-C, Gallagher KP, Nguyen N, Petry NA, Rogers WL. Myocardial clearance kinetics of technetium-99m-SQ30217: a marker of regional myocardial blood flow. J. Nucl. Med 1990;31:1183–1190. [PubMed: 2362197]

Terry, JA.; Tsui, BMW.; Perry, JR.; Hendricks, JL.; Gullberg, GT. The design of a mathematical phantom of the upper human torso for use in 3-D SPECT imaging research. In: Clarke, DCM a AM., editor. Biomedical Engineering: Opening New Doors. New York: University Press; 1990. p. 1467-1474.

Tsui BM, Frey EC, LaCroix KJ, Lalush DS, McCartney WH, King MA, Gullberg GT. Quantitative myocardial perfusion SPECT. J. Nucl. Cardiol 1998;5:507–522. [PubMed: 9796898]

Tsui BMW, Zhao XD, Gregoriou GK, Lalush DS, Frey EC, Johnson RE, McCartney WH. Quantitative cardiac SPECT reconstruction with reduced image degradation due to patient anatomy. IEEE Trans. Nucl. Sci 1994;41:2838–2844.

Welch AE, Smith AM, Gullberg GT. An investigation of the effect of finite system resolution and photon noise on the bias and precision of dynamic cardiac SPECT parameters. Med. Phys 1995;22:1829–1836. [PubMed: 8587537]

Wilson DW, Tsui BMW, Barrett HH. Noise properties of the EM algorithm: II Monte Carlo simulations. Phys. Med. Biol 1994;39:847–871. [PubMed: 15552089]

Zeng GL, Gullberg GT, Huesman RH. Using linear time-invariant system theory to estimate kinetic parameters directly from projection measurements. IEEE Trans. Nucl. Sci 1995;42:2339–2346.
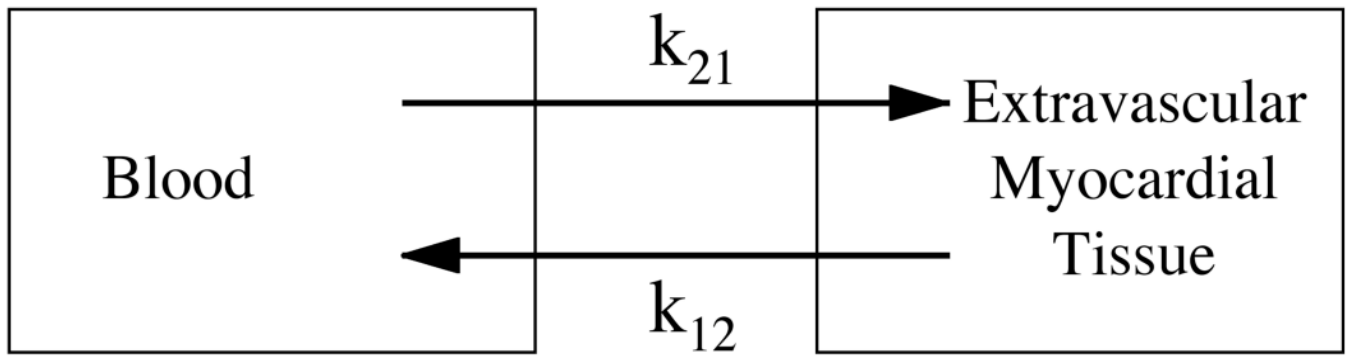
Figure 1.
A two-compartment model for the wash-in (k_{21}) and wash-out (k_{12}) of teboroxime between the blood and the extravascular myocardial tissue.
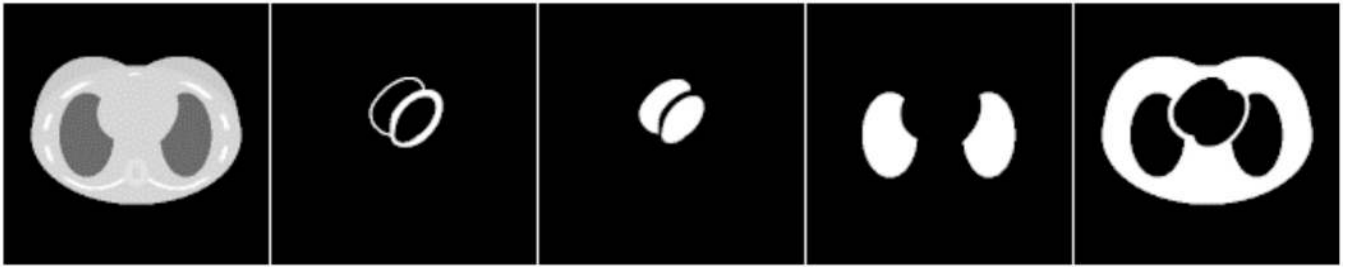
Figure 2.
Example transaxial images of the MCAT phantom (from left to right): attenuation map, myocardium, heart blood pool, lungs, and soft tissue background. The liver was in more inferior slices and is not shown here.
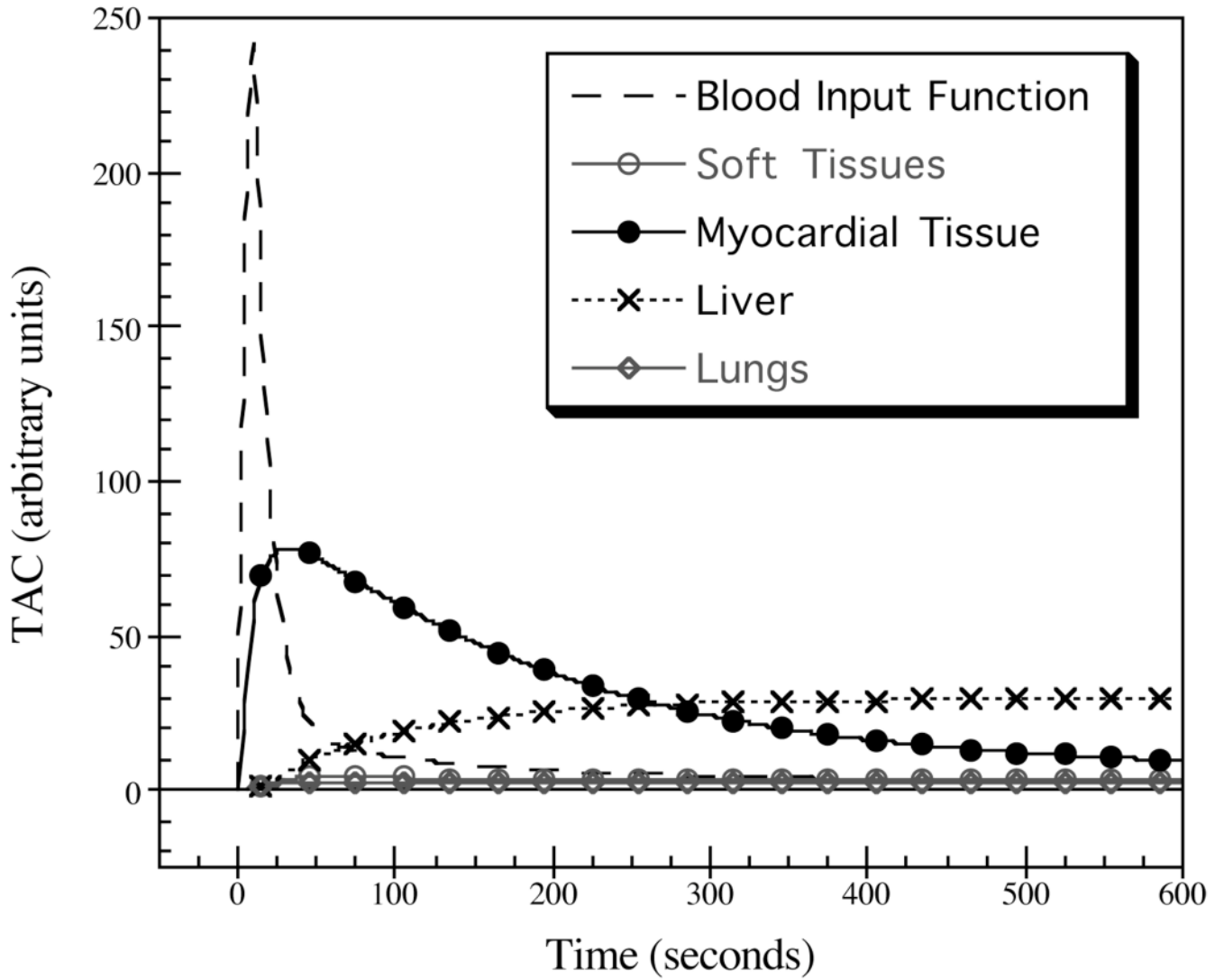
Figure 3.
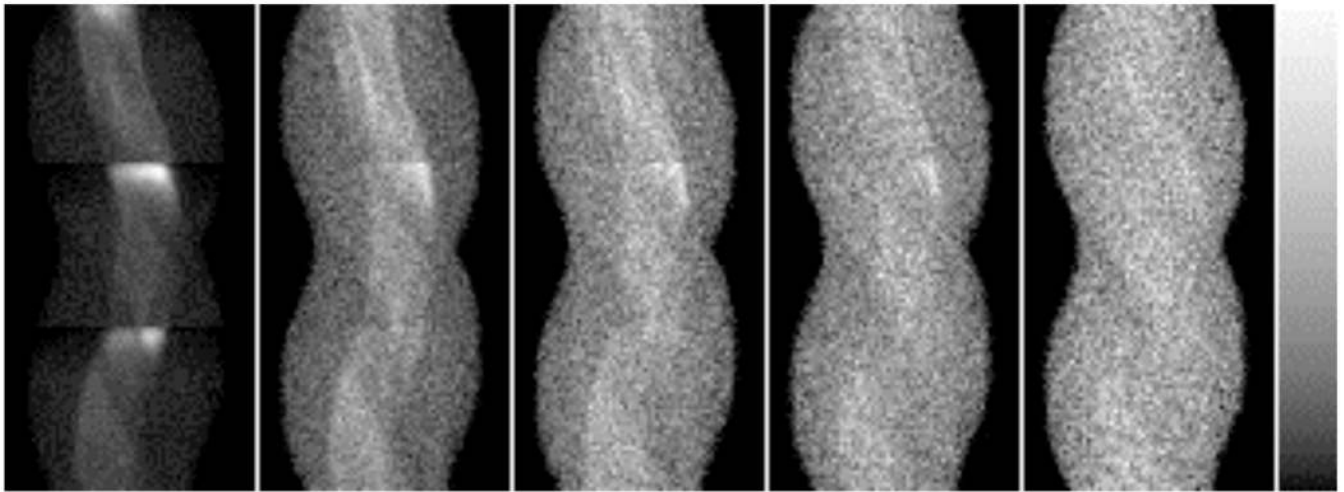Simulated time-activity curves for teboroxime as used to form the dynamic MCAT phantom.

Figure 4.
Simulated noisy sinograms for a single slice of the dynamic phantom as acquired over the following timeframes (left to right): 0–120 sec., 120–240 sec., 240–360 sec., 360–480 sec., and 480–600 sec. This example of a slow-rotation dynamic acquisition was chosen to demonstrate the inconsistent projection phenomenon, which is most easily seen for the first timeframe—abrupt discontinuities are visible between the sections of the sinogram acquired by each of the three camera heads.
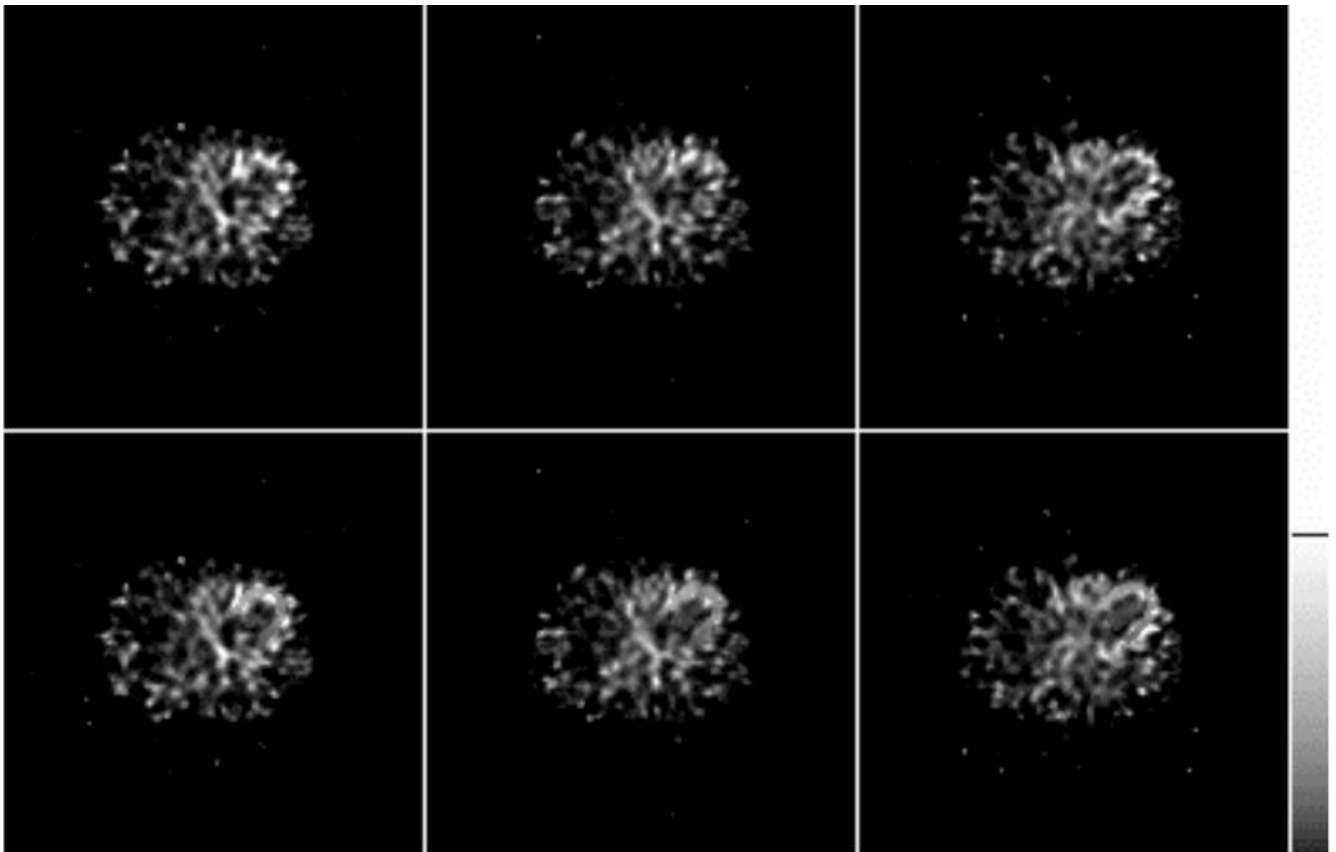
Figure 5.
Example transaxial reconstructed images of a dynamic SPECT scan reconstructed with OSEM (top row) and OSMAP (bottom row). The images are for a single 10 second duration timeframe acquired 6 minutes after injection of 540 MBq (18 mCi) Tc-99*m* teboroxime, and no post-reconstruction filter has been applied. Differences in the uniformity and definition of the myocardial wall between OSMAP and OSEM can be visualized in these images.
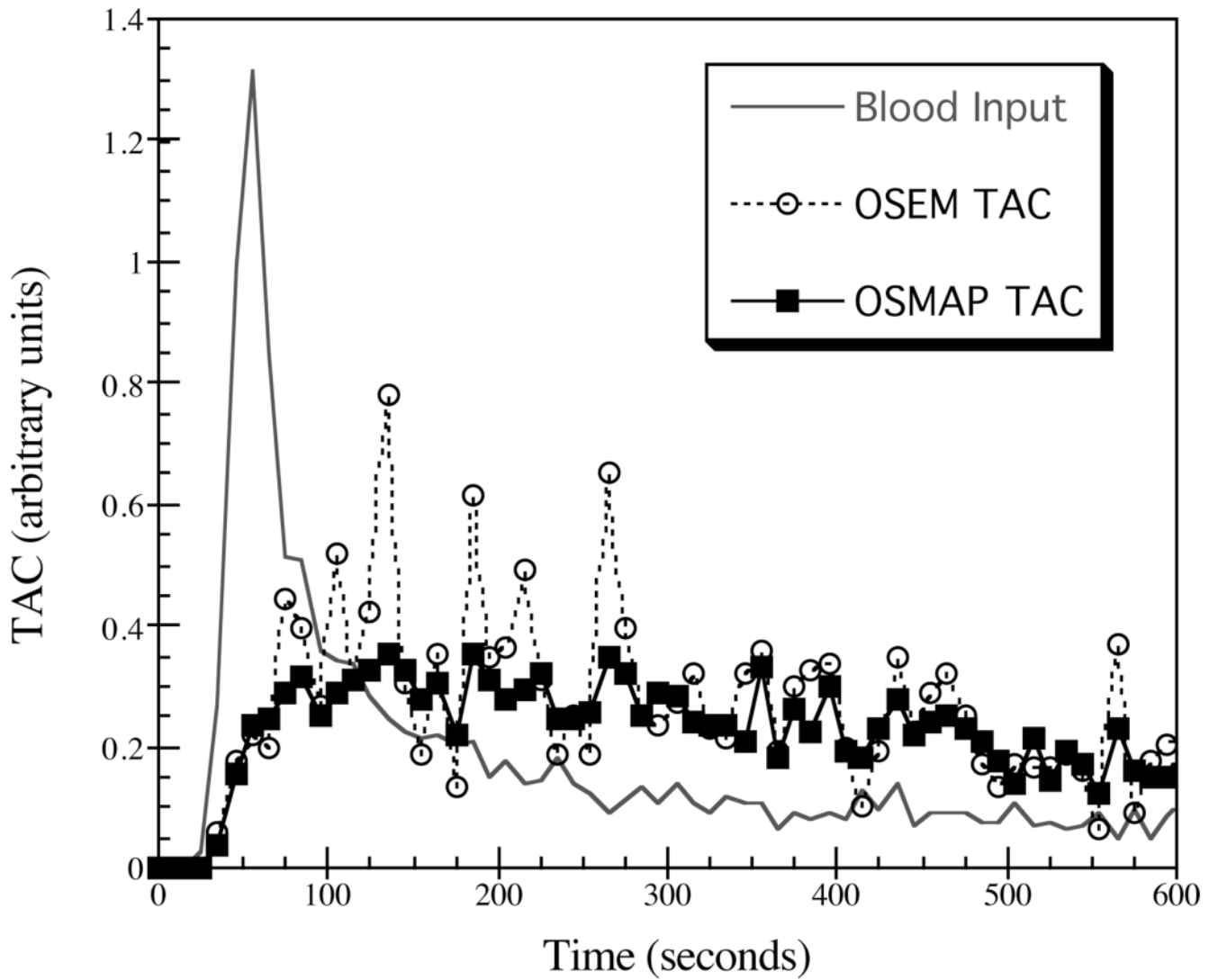
Figure 6.
Example time-activity curves for one LV region for a dynamic SPECT teboroxime patient
study obtained under pharmacologic stress. The TAC for the OSMAP algorithm appears
considerably smoother and much better defined than does the one from the OSEM data. This
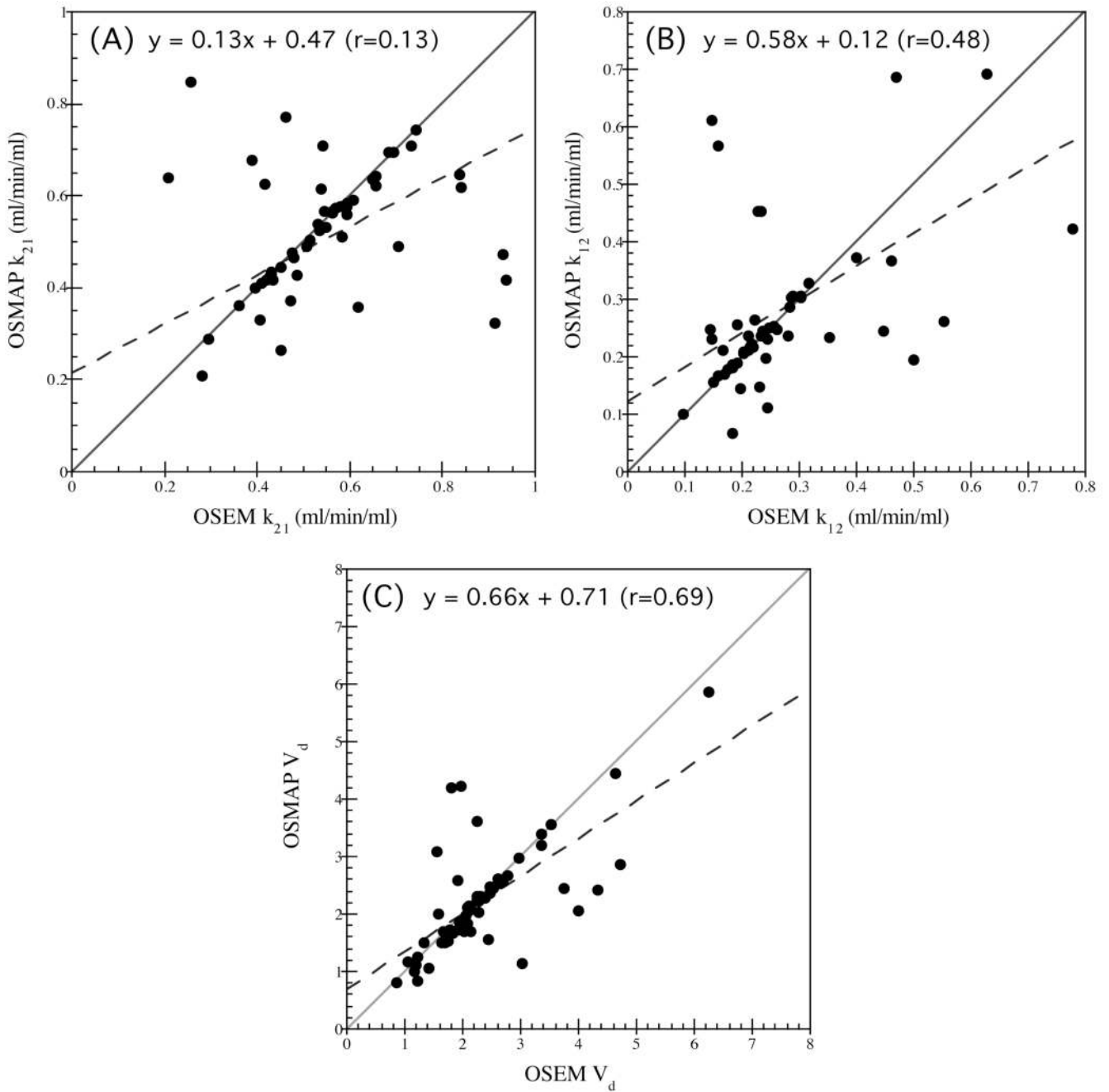effect was observed for all regions of the left ventricle.

Figure 7.
Scatter plots of wash-in (A), wash-out (B), and distribution volume (C) for one of the patient studies calculated using the dynamic OSMAP algorithm versus conventional OSEM processing. The line of identity is shown on each plot (solid, light gray), and the results of linear correlation analysis for each case are also shown.
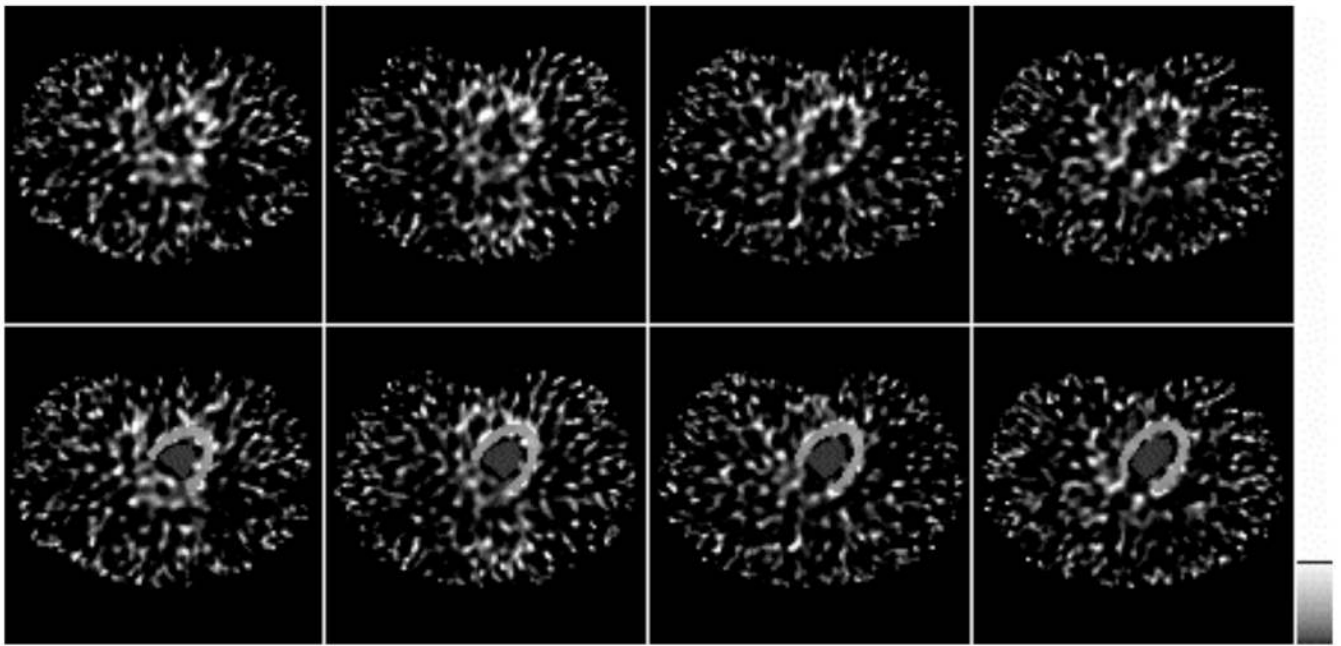
Figure 8.
Example transaxial slices through the heart for the simulation experiment reconstructed using conventional OSEM (top row) and the dynamic OSMAP algorithm (bottom row). The data are for the 30 × 20 sec. acquisition protocol, and the reconstructed timeframe shown is at 5 min. 10 sec. post-injection. The OSMAP images show greatly improved uniformity across the left ventricle where the compartmental-model based prior was defined.
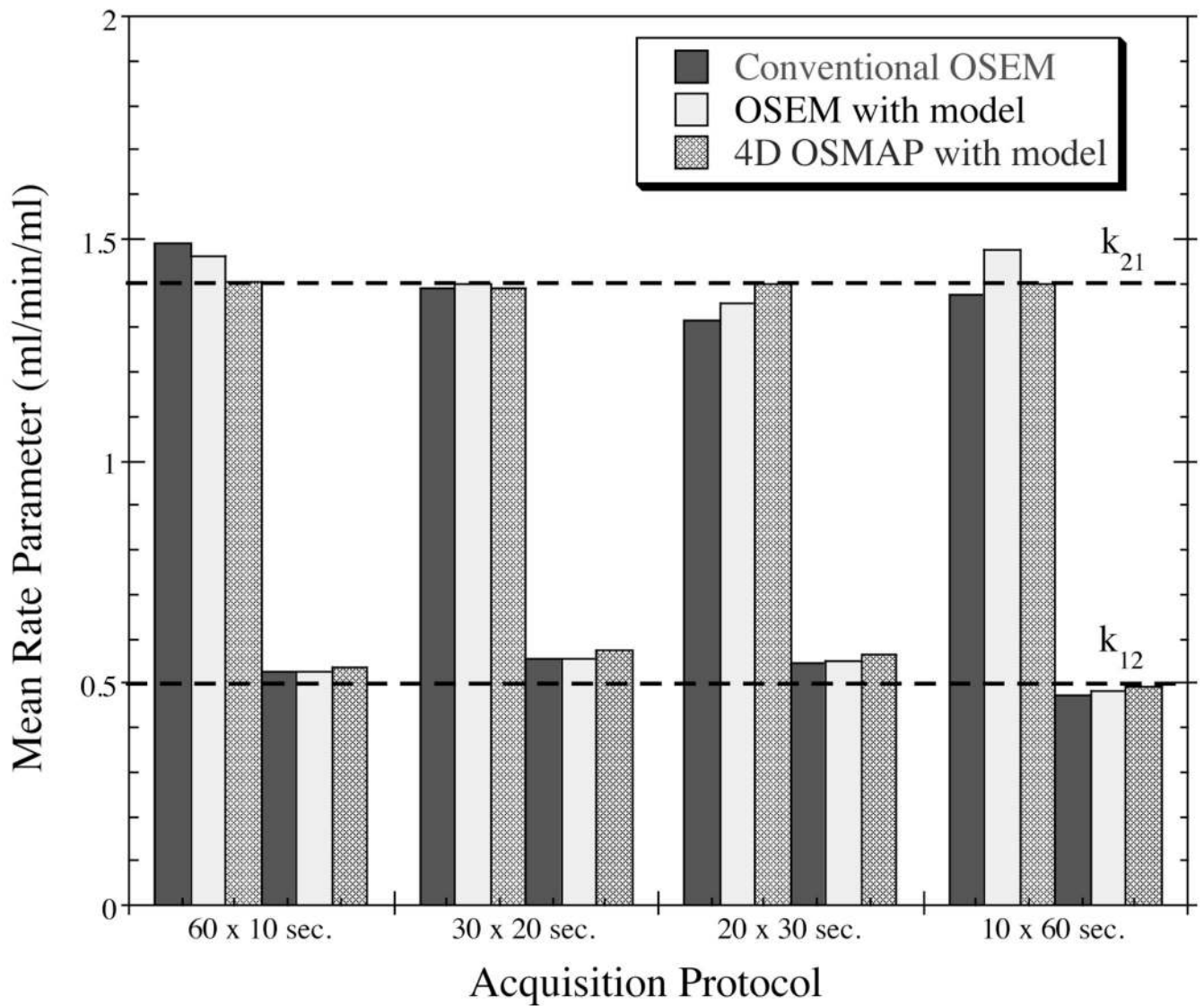
Figure 9.
Mean wash-in (k_{21}) and wash-out (k_{12}) rate parameter estimates for each of the three reconstruction methods obtained from the simulation studies. Additional information regarding the parameter estimates is provided in Table I.
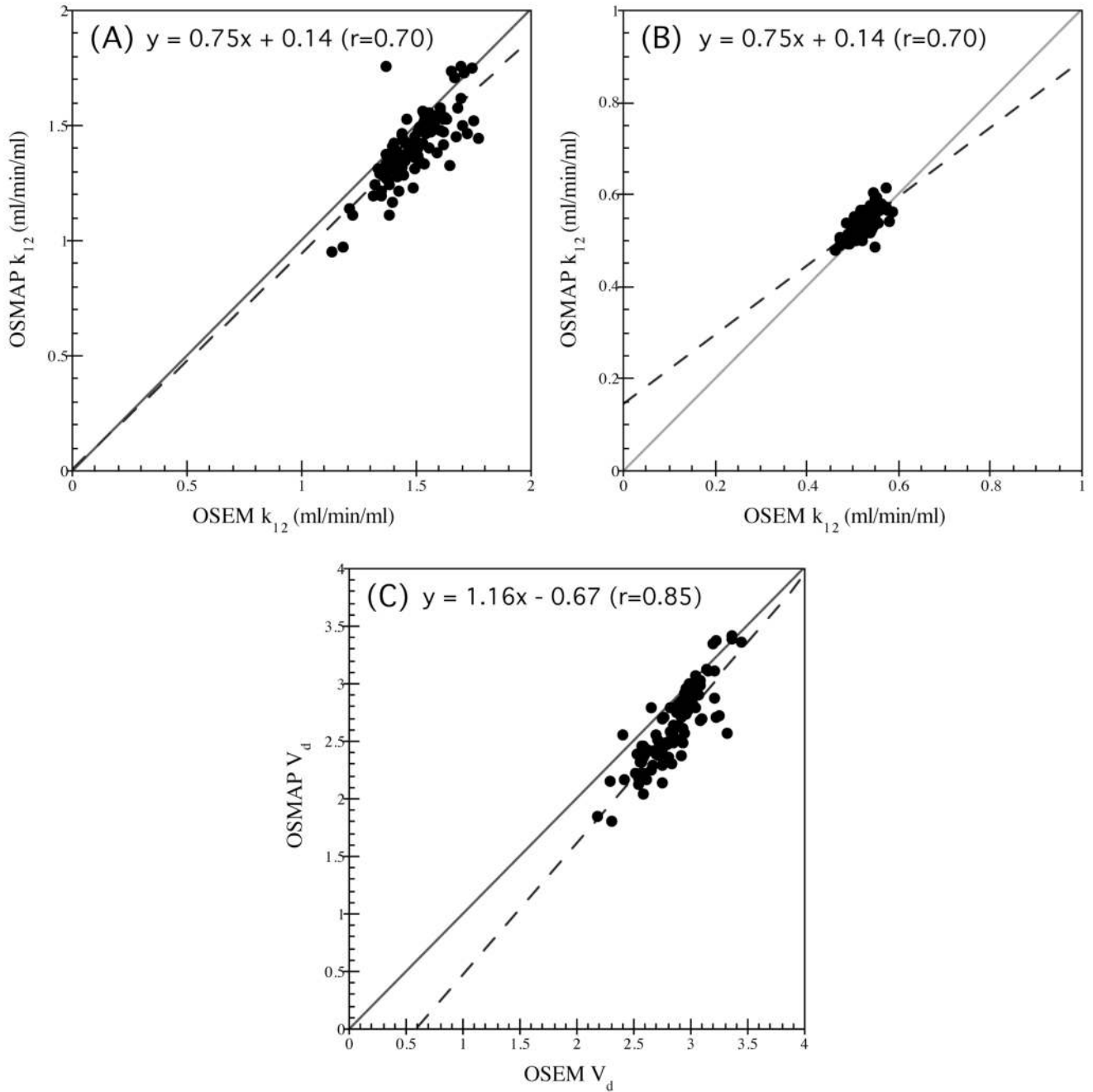
Figure 10.
Scatter plots of wash-in (A), wash-out (B), and distribution volume (C) for the simulation experiment with 60×10 sec. acquisition protocol using the dynamic OSMAP algorithm versus conventional OSEM processing. The line of identity is shown on each plot (solid, light gray), and the results of linear correlation analysis for each case are also shown.
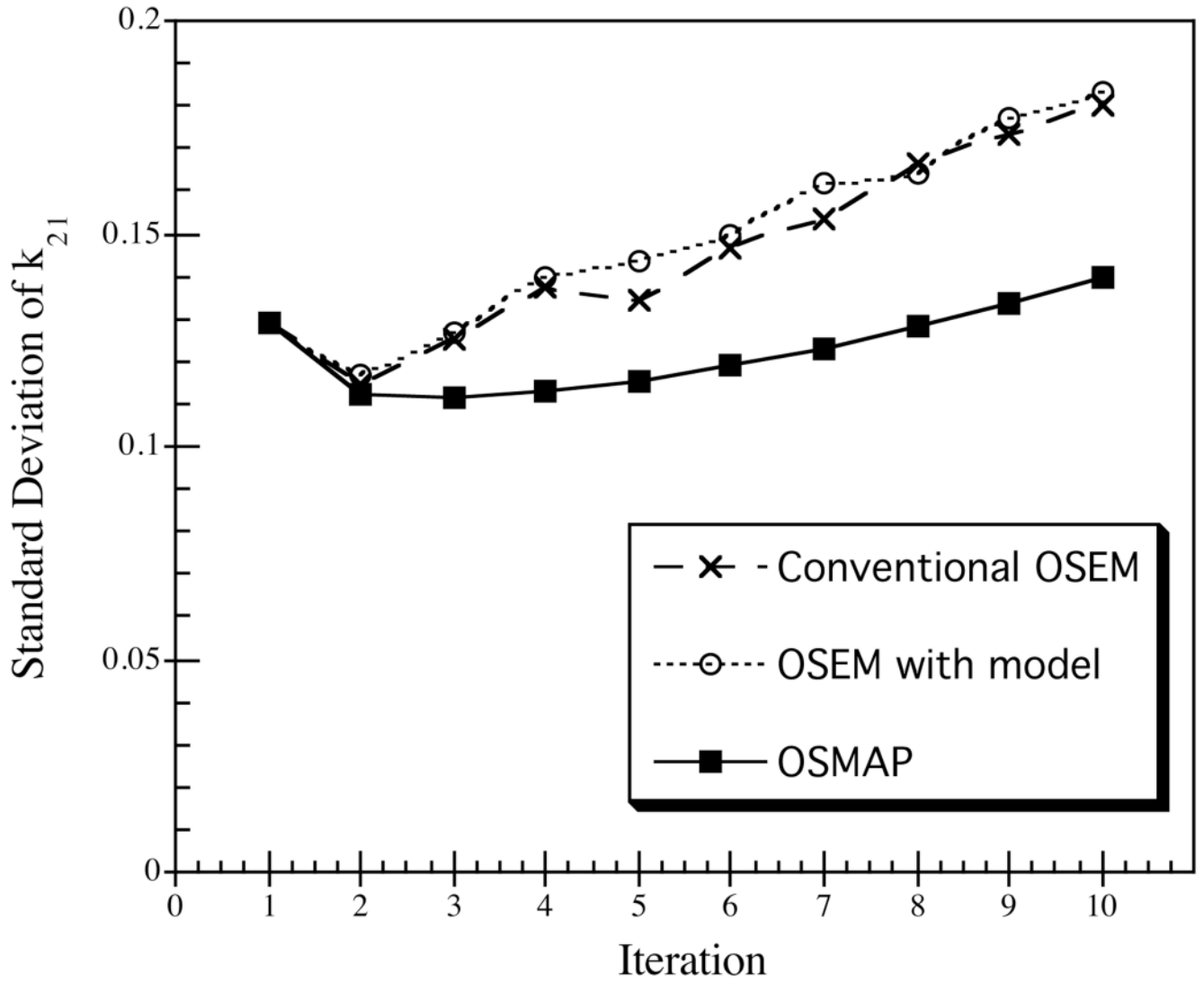
Figure 11.
Standard deviation of wash-in estimates for each algorithm plotted as a function of iteration. The OSMAP curve shows less dependence upon iteration, and provides lower uncertainty at all iterations. The data are for the 30×20 sec. acquisition protocol.

Table I

Kinetic parameter estimates and error analysis for the simulation experiments.

Protocol & Algorithm	mean k_{21} ± s.d. (ml/min/ml)	Attained sig. level[†]	k_{21} ANR[‡]	mean k_{12} ± s.d. (ml/min/ml)	Attained sig. level[†]	k_{21} ANR[‡]
True Values	1.400			0.500		
60 timeframes, 10 sec. each:						
Conventional OSEM	1.491 ± 0.129	p<0.001	0.857	0.524 ± 0.025	p<0.001	0.906
OSEM with model	1.463 ± 0.121	p<0.001	0.879	0.528 ± 0.025	p<0.001	0.897
4D OSMAP w/ model	1.402 ± 0.151	NS	0.901	0.535 ± 0.027	p<0.001	0.882
30 timeframes, 20 sec. each:						
Conventional OSEM	1.390 ± 0.134	NS	0.906	0.556 ± 0.054	p<0.001	0.801
OSEM with model	1.400 ± 0.127	NS	0.917	0.554 ± 0.052	p<0.001	0.808
4D OSMAP w/ model	1.388 ± 0.141	NS	0.901	0.573 ± 0.053	p<0.001	0.773
20 timeframes, 30 sec. each:						
Conventional OSEM	1.317 ± 0.208	p<0.001	0.819	0.545 ± 0.061	p<0.001	0.810
OSEM with model	1.355 ± 0.218	p<0.025	0.838	0.549 ± 0.059	p<0.001	0.807
4D OSMAP w/ model	1.398 ± 0.216	NS	0.865	0.562 ± 0.057	p<0.001	0.786
10 timeframes, 60 sec. each:						
Conventional OSEM	1.372 ± 0.575	NS	0.695	0.472 ± 0.079	p<0.001	0.814
OSEM with model	1.477 ± 0.661	p<0.200	0.642	0.482 ± 0.076	P<0.015	0.837
4D OSMAP w/ model	1.398 ± 0.593	NS	0.701	0.493 ± 0.079	NS	0.853

[†] Attained significance indicating that the estimates are inaccurate, NS: not significant;

[‡] ANR: accuracy-to-noise ratio